

Magnetic Field Configuration at the Galactic Center Investigated by Wide Field Near-Infrared Polarimetry

Shogo Nishiyama^{1,2}, Motohide Tamura², Hirofumi Hatano³, Saori Kanai³, Mikio Kurita³, Shuji Sato³, Noriyuki Matsunaga¹, Tetsuya Nagata¹, Takahiro Nagayama¹, Ryo Kandori², Yasushi Nakajima², Nobuhiko Kusakabe⁴, Yaeko Sato⁴, James H. Hough⁵, Koji Sugitani⁶, and Haruyuki Okuda⁷

ABSTRACT

We present a polarimetric map of a $20' \times 20'$ area toward the Galactic center. The polarization of point sources has been measured in the J , H , and K_S bands using the near-infrared polarimetric camera SIRPOL on the 1.4 m telescope IRSF. One percent or better accuracy of polarization degree is achieved for sources with $J < 14.5$, $H < 13.5$, and $K_S < 12.0$. Comparing the Stokes parameters between high extinction stars and relatively low extinction ones, we have obtained a polarization originating from magnetically aligned dust grains at the central region of our Galaxy of at most 1–2 kpc. The distribution of the position angles shows a peak at $\sim 20^\circ$, nearly parallel to the Galactic plane, suggesting a toroidal magnetic configuration. The derived direction of the magnetic field is in good agreement with that obtained from far-infrared/submillimeter observations, which detect polarized thermal emission from dust in the molecular clouds at the Galactic center. Our results show that by subtracting foreground components, near-infrared polarimetry allows investigation of the magnetic field structure at the Galactic center.

Subject headings: Galaxy:center — dust,extinction — polarization — infrared:ISM — ISM:magnetic fields

1. INTRODUCTION

The discovery of polarized radio emission extending perpendicular to the Galactic plane, such as nonthermal radio filaments (Yusef-Zadeh et al. 1984) and polarized plumes (Tsuboi et al. 1986),

has provided early evidence for a substantial poloidal component of the magnetic field in the central region of our Galaxy. High resolution observations at radio wavelengths have revealed more filaments of similar orientations (e.g., LaRosa et al. 2004; Yusef-Zadeh et al. 2004), where the magnetic fields were found to be predominantly aligned along the filaments. The accumulation of these observational results has led to the hypothesis that most of the volume of the Galactic center (GC) is permeated by a *poloidal* magnetic field.

Evidence for the existence of a *toroidal* magnetic structure comes from far-infrared (FIR) and submillimeter (sub-mm) observations, which detect polarized thermal emission from magnetically aligned dust grains. The rotation axis of the dust grain aligns with the magnetic field, and thus the polarization of the thermal emission indicates the magnetic field direction (the measured direction of the E-vector is orthogonal to the magnetic field).

¹Department of Astronomy, Kyoto University, Kyoto 606-8502, Japan; shogo@kustro.kyoto-u.ac.jp

²National Astronomical Observatory of Japan, Mitaka, Tokyo 181-8588, Japan

³Department of Astrophysics, Nagoya University, Nagoya 464-8602, Japan

⁴Department of Astronomical Sciences, Graduate University for Advanced Studies (Sokendai), Mitaka, Tokyo 181-8588, Japan

⁵Centre for Astrophysics Research, University of Hertfordshire, Hatfield, Herts AL10 9AB, UK

⁶Graduate School of Natural Sciences, Nagoya City University, Nagoya 467-8501, Japan

⁷Institute of Space and Astronautical Science, Japan Aerospace Exploration Agency, Sagami-hara, Kanagawa 229-8510, Japan

The magnetic fields inferred from these observations (e.g., Werner et al. 1988; Morris et al. 1992; Hildebrand et al. 1993) run parallel to the Galactic plane. Recent linear polarization observations of the 450- μm continuum suggest a large-scale toroidal magnetic field extending over a region of 170×30 pc (Novak et al. 2003).

Chuss et al. (2003) found an interesting dependence of the magnetic field direction on the sub-mm flux. In low density regions, the field aligns generally perpendicular to the Galactic plane, while in high density regions, the field has a toroidal geometry. One explanation for this is that the global magnetic field in the early Galaxy was initially in a poloidal configuration, however the gravitational energy density in dense molecular clouds was strong enough to distort the poloidal field into a toroidal one, though it was insufficient in the low density regions.

A model which can connect the poloidal and toroidal magnetic fields was proposed by Uchida et al. (1985), and was extended to a more realistic case by Shibata & Uchida (1986). This magnetohydrodynamic model was developed to explain the GC lobes found by Sofue & Handa (1984). Since magnetic flux is generally frozen into matter, differential rotation and infall can shear an initially poloidal field into a toroidal one. Consequently, a toroidal field is developed close to the Galactic plane, while the field is vertical at high Galactic latitude.

The Uchida et al. (1985) model predicts that the toroidal component will generally be more dominant closer to the Galactic plane. A map of the direction of the magnetic field could therefore be a simple indicator of how well this model works in the GC. However, dust emissivity is high in dense, warm clouds, and thus observations of dust emission in FIR/sub-mm wavelengths are strongly limited to such regions, which show patchy distributions in the GC region.

In this paper, we present near-infrared (NIR) polarimetry of point sources toward the GC covering a much larger region of the sky than previous observations of this region. We demonstrate that NIR polarization can provide information on the magnetic field structure not only in the Galactic disk, but also in the central region of our Galaxy.

2. OBSERVATIONS AND DATA REDUCTION

We conducted NIR polarimetric observations of the GC with the SIRPOL camera on the night of 4 July 2006. SIRPOL consists of a single-beam polarimeter (a half-wave plate rotator unit and a fixed wire-grid polarizer; Kandori et al. 2006) and the NIR imaging camera SIRIUS (Simultaneous Infrared Imager for Unbiased Survey; Nagashima et al. 1999; Nagayama et al. 2003), and is attached to the 1.4-m telescope IRSF (Infrared Survey Facility). SIRPOL provides images of a $7'.7 \times 7'.7$ area of sky in three NIR wavebands, J ($1.25\mu\text{m}$), H ($1.63\mu\text{m}$), and K_S ($2.14\mu\text{m}$), simultaneously. The detectors are three 1024×1024 HgCdTe arrays, with a scale of $0''.45$ pixel $^{-1}$. The filter system of IRSF/SIRPOL is similar to the MKO system (Tokunaga et al. 2002).

We observed a $20' \times 20'$ area (nine SIRPOL fields) centered at the position of Sgr A* ($17^{\text{h}}45^{\text{m}}40.0^{\text{s}}$, $-29^{\circ}00'28''.0$; J2000.0). We took 10-s exposures each at 4 wave plate angles ($0^{\circ}0$, $22^{\circ}5$, $45^{\circ}0$, $67^{\circ}5$) at each of 10 dithered positions. The weather condition was photometric, with a seeing of $\sim 1''.2$ (J), $\sim 1''.1$ (H), and $\sim 1''.0$ (K_S). The IRAF (Image Reduction and Analysis Facility)¹ software package was used to perform dark- and flat-field corrections, followed by sky background estimation and subtraction.

3. DATA ANALYSIS AND RESULTS

3.1. Polarization of Point Sources

To obtain the photometric magnitudes and errors in the three bands, we used the DAOFIND task in the DAOPHOT package (Stetson 1987) to identify point sources in Stokes I images [$I = (I_{0^{\circ}} + I_{22^{\circ}5} + I_{45^{\circ}} + I_{67^{\circ}5})/2$]. The sources were then input to the ALLSTAR task for PSF-fitting photometry. About 10 sources were used to construct the PSF in each image. Each Stokes I image was calibrated with the photometric image of the same position obtained in previous imaging observations (Nishiyama et al. 2006a), in which the standard star #9172 (Persson et al. 1998) was

¹ IRAF is distributed by the National Optical Astronomy Observatory, which is operated by the Association of Universities for Research in Astronomy, Inc., under cooperative agreement with the National Science Foundation.

used for calibration. We assumed that #9172 has magnitudes of $J = 12.48$, $H = 12.12$, and $K_S = 12.03$ in the IRSF/SIRIUS system.

In Fig. 1 we show the $H - K_S$ histogram (top panel) and the JHK_S color-color diagram (bottom panel) for stars with photometric errors of less than 0.11 mag. Also plotted are loci of unreddened giants and dwarfs. The arrow is parallel to the reddening vector, and its length corresponds to $A_{K_S} = 1$ mag (Nishiyama et al. 2006a). Considering large extinction toward the GC, stars with small $H - K_S$ should be attributed to foreground (disk) stars, and stars consisting of the strongest peak in the $H - K_S$ histogram is attributed to ones in the Galactic bulge.

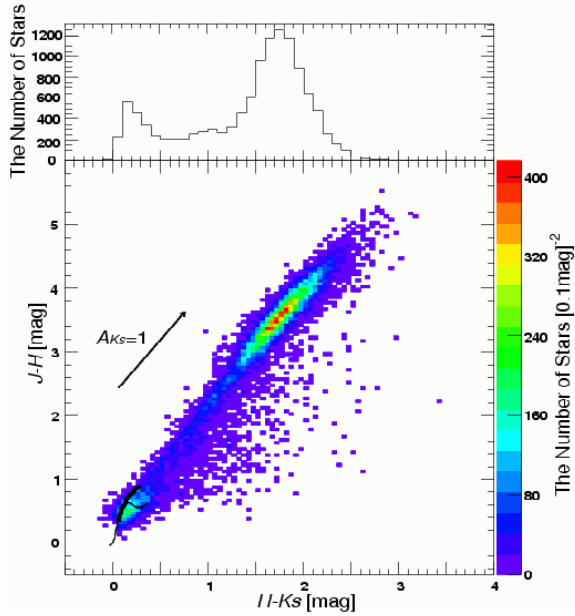


Fig. 1.— $H - K_S$ histogram (top) and JHK_S color-color diagram (bottom) for point sources with J , H , and K_S photometric errors of less than 0.11 mag. The thick and thin curves represent the loci of giants and dwarfs, respectively (Tokunaga 2000). The arrow indicates the $A_{K_S} = 1$ mag reddening vector (Nishiyama et al. 2006a).

Astrometric calibration was performed, field by field, with reference to the positions of point sources in the 2MASS point source catalog (Skrutskie et al. 2006). Sources with photometric errors of less than 0.05 mag in 2MASS and our catalog were

used for the calibration. As a result of this astrometric calibration, we obtained an rms of the positional difference of better than $0''.1$ for sources with a < 0.11 mag photometric error.

The Stokes parameters I , Q , and U for point sources were determined from aperture polarimetry of combined images as follows. DAOFIND and APPHOT tasks were used for the point-source identification and the aperture photometry. We then obtained the intensity for each wave plate angle (I_{0° , $I_{22.5^\circ}$, I_{45° , $I_{67.5^\circ}$). Since aperture photometry with a small aperture radius gives a better photometric result than PSF-fitting photometry, aperture photometry was applied in the following procedure. The size of the PSF is slightly different among the four images due to variations of the seeing, hence we used different apertures for each image. The aperture diameters were set to be equal to $2 \times$ FWHMs of the best fit Gaussian profile (GFWHM) determined by the PSFMESURE task. The means of the adopted aperture sizes were $\sim 1''.2$ (J), $\sim 1''.1$ (H), and $\sim 1''.0$ (K_S). The position angle offset of SIRPOL α was estimated to be $\alpha = 105^\circ$ (Kandori et al. 2006) which was set to the origin of the angles 0° , 22.5° , 45° , and 67.5° . Based on the intensities of the four angles, we calculated the total intensity I and two “raw” Stokes parameters Q' and U' as

$$\begin{aligned} I &= (I_{0^\circ} + I_{22.5^\circ} + I_{45^\circ} + I_{67.5^\circ})/2, \\ Q' &= I_{0^\circ} - I_{45^\circ}, \\ U' &= I_{22.5^\circ} - I_{67.5^\circ}. \end{aligned}$$

The polarization degree P and the position angle θ were derived by

$$\begin{aligned} P &= \sqrt{(Q'^2 + U'^2)}/I, \\ \theta &= \frac{1}{2} \arctan(U'/Q'), \end{aligned}$$

where

$$Q = Q' \cos(2\alpha) - U' \sin(2\alpha), U = Q' \sin(2\alpha) + U' \cos(2\alpha). \quad (1)$$

The debiased P was finally derived by $P_{\text{db}} = \sqrt{P^2 - \delta P^2}$ where δP is the error of P , given by

$$\delta P = \frac{1}{P} \sqrt{\left(\frac{Q'}{I}\right)^2 \left[\delta\left(\frac{Q'}{I}\right)\right]^2 + \left(\frac{U'}{I}\right)^2 \left[\delta\left(\frac{U'}{I}\right)\right]^2}. \quad (2)$$

We regard sources for which $(P^2 - \delta P^2) \leq 0$ as non-polarized source, and we do not consider such

sources further in this paper. The typical magnitudes for $\delta P = 1\%$ are 14.5 (J), 13.5 (H), and 12.0 (K_S).

Fig. 2 plots the degree and position angle of stars with a degree of polarization determined to have an accuracy better than 1%. The orientation of each bar gives the inferred direction of polarization and the length of the bar is proportional to the degree of polarization. The coordinate offsets ($'$) were measured with respect to the location of Sgr A*.

Histograms of debiased P and θ in each band are shown in Fig. 3. The mean degree and angle are 6.3 % and 8° in the J band, 6.2 % and 13° in the H band, and 4.3 % and 14° in the K_S band. Kobayashi et al. (1980) detected K -band emission of unresolved point sources at the central $7' \times 7'$ region and obtained an average degree of polarization of 5%, with position angles of 10° to 15° , showing a good agreement with our results in the K_S band.

The correlation between θ in the K_S band and $H - K_S$ color is shown in Fig. 4. To clarify the dependence of θ on $H - K_S$, we divided the $H - K_S$ data set in bins of equal size (0.5 mag) and calculated the mean and the standard deviation of θ in each bin, represented by red crosses in Fig. 4. We can see a change of the mean position angle at $H - K_S \sim 1.0$: the mean angle is $\sim 5^\circ$ at $0 < H - K_S < 1.0$, while it is $\sim 15^\circ$ at $H - K_S > 1.0$. Such a change has already been indicated by Kobayashi et al. (1983), and is also in good agreement with their results.

We have identified two distinct populations in Fig. 3: stars with small P and small θ (typically $P_J \lesssim 5\%$ and $\theta \lesssim 0^\circ$), and stars with larger P and $\theta \gtrsim 10^\circ$ (see also Fig. 4). It is conceivable that the former are nearby stars, and the latter are stars distributed in the Galactic bulge. The stars that corresponds to the strong peak in the P_J histogram at $\sim 2\%$ have a color of $H - K_S \sim 0.1-0.2$ (see also Fig. 1) and $\theta_J \sim 0^\circ$ and thus are most likely to be nearby dwarfs. This peak can be found in the H band around $P_H \sim 1\%$, but becomes invisible in the P_{K_S} histogram. In the K_S band, most of the stars detected are red giants in the Galactic bulge, which constitute a strong peak in the P_{K_S} histogram. The strong peak at $P_{K_S} \sim 4\%$ corresponds to those at $\sim 7\%$ in P_H , and at $\sim 10\%$ in P_J , because this change of degree of polarization

can be explained by the power law $P_\lambda \propto \lambda^{-2}$ of the interstellar polarization (Nagata et al. 1994). The distinct populations, and the wavelength dependence of the polarization will be discussed in another paper (H. Hatano et al., in preparation).

Since the vector maps in Fig. 2 are crowded and thus almost illegible, we show the K_S -band mean vector map in Fig. 5. The mean degree and position angles were calculated using stars in a $0'.8 \times 0'.8$ grid with $P_{K_S}/\delta P_{K_S} > 3.0$. The vectors are superposed on the three color (J, H, K_S) composite image of the same region. At a first glance, most of the vectors are in order, which can also be seen in the θ_{K_S} histogram, and are nearly parallel to the Galactic plane. Moving north-eastward across the image, the position angles slightly rotate clockwise. At a few positions where the number density of stars is small, and hence strong foreground extinction exists, the vectors have irregular directions, particularly at the northwestern corner. These irregularities might be explained by the inherent magnetic field configuration in foreground dark clouds.

3.2. Separating Foreground Polarization and Galactic Center Component

Polarization vectors of stars trace the plane-of-the-sky projection of the magnetic field, and polarimetric measurements of stars of different distances reveal the three-dimensional distribution of the magnetic field orientations. In our observed fields, we can detect stars in the Galactic disk and bulge. From the stars at the close side in the Galactic bulge (referred to hereafter as “blue stars” due to their relatively small reddening), we can obtain the degree of polarization and position angle, which are affected mainly by interstellar dust in the Galactic disk. The light from stars at the far side in the bulge (hereafter “red stars”) is transmitted through the dust in the disk and the bulge. Therefore, using both blue and red stars, we can obtain the bulge (GC) component of the polarization. The procedure is as follows. (In the following process, only K_S -band polarization of stars is used.)

As a first step, we divided the field into 10×10 sub-fields of $2' \times 2'$ and drew $H - K_S$ histograms for each sub-field with stars of $\delta H < 0.11$, $\delta K_S < 0.11$, and $H \leq 15.0$, which are much brighter than the 10σ limiting magnitude in the H band

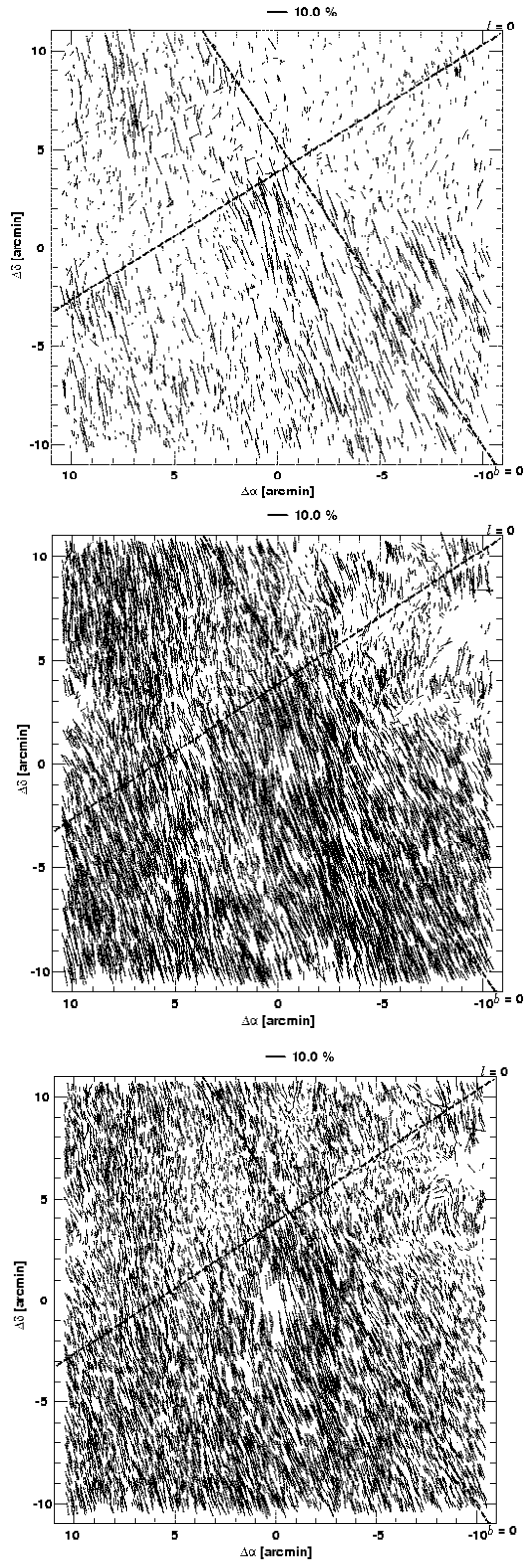


Fig. 2.— Polarization of the Galactic center for stars with $P > 0\%$ and $\delta P < 1\%$. 2243, 7963, and 9661 stars in the J (top), H (middle), and K_S (bottom) bands, respectively, are plotted. The coordinate offsets (l') were measured with respect to the location of Sgr A*. Each bar is drawn parallel to the E-vector of the measured polarization. This is the direction of the $l = 0$ line.

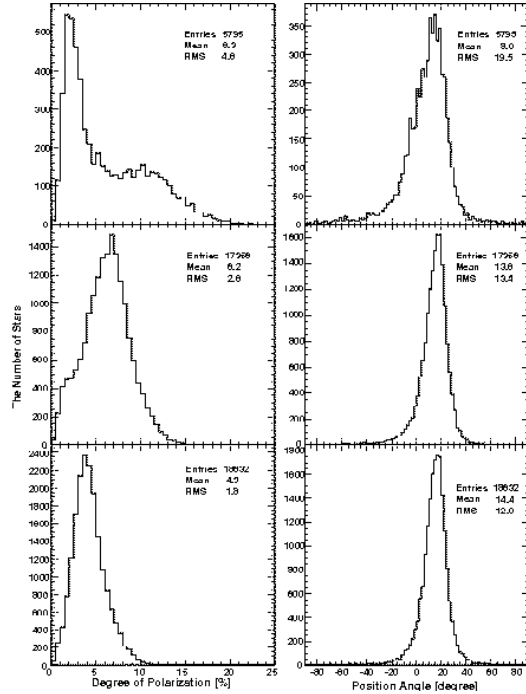


Fig. 3.— Histograms of degree of polarization (left) and position angle (right) in the J (top), H (middle), and K_S (bottom) bands, for stars with $P > 0\%$ and $\delta P < 3\%$. 5795 (J), 17356 (H), and 18632 (K_S) stars are employed in these histograms.

(16.7 mag). One of the $H - K_S$ histograms is shown in Fig. 6, upper left panel. Using the histograms, we evaluated a peak value of the histogram $(H - K_S)_{\text{peak}}$ for each sub-field. Fig. 7 is an H vs. $H - K_S$ color-magnitude diagram (CMD) for stars with $\delta H < 0.11$ and $\delta K_S < 0.11$. This CMD shows that the criterion $H \leq 15.0$ is bright enough to avoid the influence of the limiting magnitudes ($H \approx 16.7$, $K_S \approx 15.5$) on the determination of $(H - K_S)_{\text{peak}}$.

Using the $H - K_S$ color, we divided the stars with $\delta P < 3\%$ into three sub-groups: “nearby” stars and “blue” and “red” stars in the bulge. We assume that nearby stars have a color of $H - K_S < 1.0$, because at $H - K_S \sim 1.0$ the number of stars drops and approaches a minimum (Fig. 1, top panel) and a clear change of position angles can be determined (Fig. 4). The “blue” stars are redder than $H - K_S = 1.0$

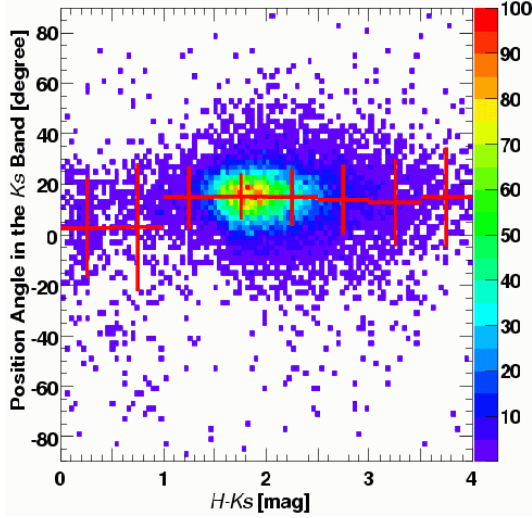


Fig. 4.— Position angle θ in the K_S band vs. $H - K_S$ diagram for stars with $\delta H < 0.11$, $\delta K_S < 0.11$, $P_{K_S} > 0\%$ and $\delta P_{K_S} < 3\%$. The red crosses represent the mean and standard deviations of θ in 0.5 mag width bins.

and bluer than $(H - K_S)_{\text{peak}}$. The stars with $H - K_S > (H - K_S)_{\text{peak}}$ are selected as “red” stars (lower left panel in Fig. 6). The average and standard deviation of $(H - K_S)_{\text{peak}}$ of the 100 sub-fields are 1.85 and 0.24, respectively; Fig. 8 shows the $H - K_S$ histogram (top panel) of the red and blue stars, and their location in the K_S vs. $H - K_S$ CMD (bottom panel). The blue stars have a peak at $H - K_S \approx 1.5$, while the red stars have a peak at $H - K_S \approx 2.0$. The red and blue stars of *all* sub-fields are plotted, so their distribution is overlapped in the CMD of Fig. 8. There are ~ 60 to ~ 340 stars with δP better than 3% in each sub-field in the K_S band.

As a second step to subtract the polarization originating in the bulge, Q'/I and U'/I histograms in the K_S band were constructed for the blue and red stars in each sub-field (upper and lower right panels in Fig. 6). We calculated their means as $\langle Q'/I \rangle_B$, $\langle Q'/I \rangle_R$, $\langle U'/I \rangle_B$, and $\langle U'/I \rangle_R$. We then obtained the degree of po-

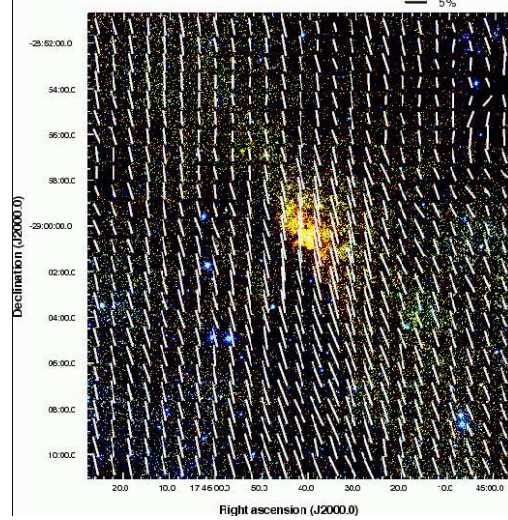


Fig. 5.— K_S -band polarization vector map superposed on the three color (J , H , K_S) composite image of the Galactic center. The Galactic center is the bright yellow blob in the center. The mean P_{K_S} and θ_{K_S} are calculated for each $0'.8 \times 0'.8$ grid. Note here that stars with $P_{K_S} > 0\%$ and $P_{K_S}/\delta P_{K_S} > 3.0$ are used for the calculation, so that the mean P_{K_S} might be overestimated.

larization and position angle for the blue stars,

$$P_B = \sqrt{\left\langle \frac{Q'}{I} \right\rangle_B^2 + \left\langle \frac{U'}{I} \right\rangle_B^2}, \quad \theta_B = \frac{1}{2} \arctan \left(\frac{\langle U'/I \rangle_B}{\langle Q'/I \rangle_B} \right),$$

and for the red stars,

$$P_R = \sqrt{\left\langle \frac{Q'}{I} \right\rangle_R^2 + \left\langle \frac{U'}{I} \right\rangle_R^2}, \quad \theta_R = \frac{1}{2} \arctan \left(\frac{\langle U'/I \rangle_R}{\langle Q'/I \rangle_R} \right).$$

where $\langle U'/I \rangle_B$ and $\langle Q'/I \rangle_B$, and $\langle U'/I \rangle_R$ and $\langle Q'/I \rangle_R$ are the Stokes parameters whose position-angle offset are corrected [see equations (1)]. We obtained P and θ for the red minus blue components using the following equations (Goodrich 1986):

$$P_{R-B} = \sqrt{\left(\left\langle \frac{Q'}{I} \right\rangle_R - \left\langle \frac{Q'}{I} \right\rangle_B \right)^2 + \left(\left\langle \frac{U'}{I} \right\rangle_R - \left\langle \frac{U'}{I} \right\rangle_B \right)^2},$$

$$\theta_{R-B} = \frac{1}{2} \arctan \left(\frac{\langle \frac{U}{I} \rangle_R - \langle \frac{U}{I} \rangle_B}{\langle \frac{Q}{I} \rangle_R - \langle \frac{Q}{I} \rangle_B} \right),$$

where $(\langle U/I \rangle_R - \langle U/I \rangle_B)$ and $(\langle Q/I \rangle_R - \langle Q/I \rangle_B)$ are also the Stokes parameters whose position-angle offset are corrected [see equations (1)]. The errors of $\langle Q'/I \rangle$ and $\langle U'/I \rangle$ were calculated from the standard error on the mean σ/\sqrt{N} of the Q'/I and U'/I histograms, where σ is the standard deviation and N is the number of stars. The error of P_{R-B} was then calculated by propagation of errors [see equation (2)].

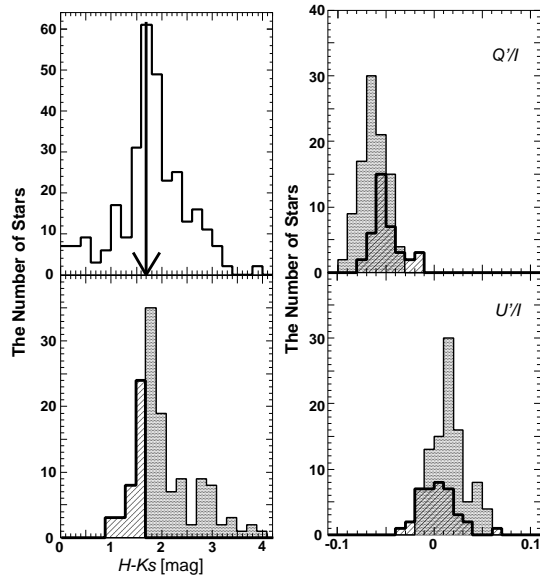


Fig. 6.— Upper left: $H - K_S$ histogram of a sub-field ($l, b = +1', -1'$) with stars with $\delta H < 0.11$, $\delta K_S < 0.11$, and $H \leq 15.0$. The arrow represents the peak of the histogram. Lower left: $H - K_S$ histograms of the same sub-field for blue (hatched) and red (dotted) stars with $P_{K_S} > 0\%$ and $\delta P_{K_S} < 3\%$. Upper and lower right: Q'/I and U'/I histograms for the blue (hatched) and red (dotted) stars shown in the lower left histogram.

We show vector maps for P_B and θ_B (blue bars) and P_R and θ_R (red bars) in Fig. 9, and the same map for P_{R-B} and θ_{R-B} in Fig. 10. The average of P_B and θ_B are 3.8% and $15^\circ 1$, and of P_R and θ_R are 4.3% and $15^\circ 0$, respectively (Fig. 11, hatched and dotted histograms). Those of P_{R-B} and θ_{R-B}

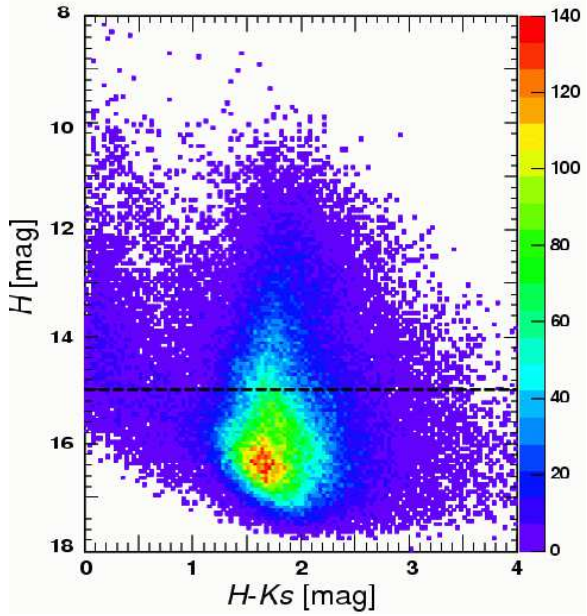


Fig. 7.— H vs. $H - K_S$ color-magnitude diagram for stars with $\delta H < 0.11$ and $\delta K_S < 0.11$. The dashed line represents $H = 15.0$.

are also obtained as 0.85% and $16^\circ 0$ (white histogram in Fig. 11), only for grids where the polarization is detected with $P_{R-B}/\delta P_{R-B} \geq 2$. The averages for θ_B and θ_{R-B} are similar, but their dispersions are different: the standard deviation of θ_B is $6^\circ 0$, while that of θ_{R-B} is $21^\circ 5$ (the average of $\delta\theta_{R-B}$ is $7^\circ 6$.) The small dispersion of θ_B suggests that the long axis of the interstellar dust grains in the Galactic disk is well aligned perpendicular to the Galactic plane. The histogram of θ_{R-B} has a peak at $\sim 20^\circ$, which also roughly coincides with the angle of the Galactic plane. A similar result is also obtained for the H -band polarization.

In Fig. 10, our P_{R-B} and θ_{R-B} are plotted overlaid on the B -vectors derived from FIR/sub-mm observations (Dotson et al. 2000; Novak et al. 2000; Chuss et al. 2003). Although the observations are restricted to the position of dense molecular clouds, we find good agreement between the FIR/sub-mm and NIR observations in spite of the difference of wavelengths and methods of deriving polarization.

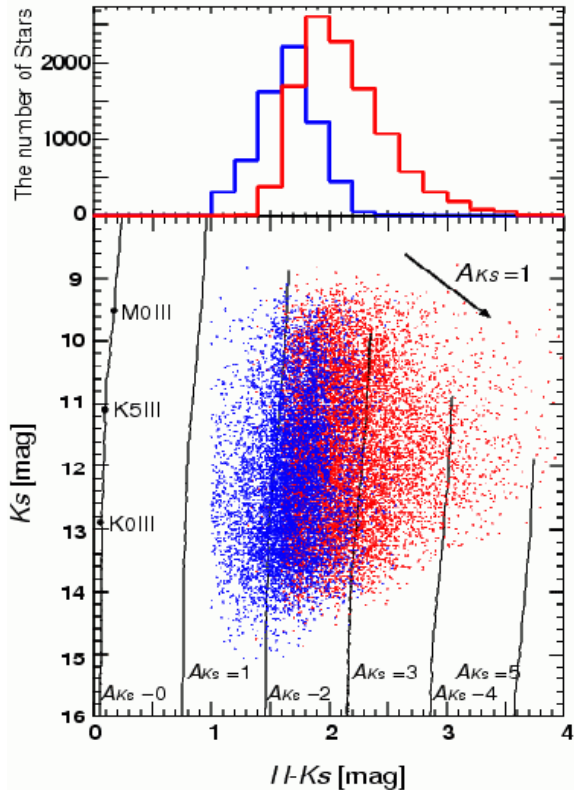


Fig. 8.— $H - K_S$ histograms (top) and K_S vs. $H - K_S$ color-magnitude diagram (bottom) for red and blue stars with $P_{K_S} > 0\%$ and $\delta P_{K_S} < 3\%$. Theoretical isochrones for different extinctions of $A_{K_S} = 0, 1, 2, 3, 4,$ and 5 mag, are shown by solid curves. The arrow indicates the $A_{K_S} = 1$ mag reddening vector (Nishiyama et al. 2006a).

4. DISCUSSION

4.1. Previous Infrared Polarimetry toward the GC

NIR polarimetry for diffuse emission and point sources toward the GC has been conducted since the 1970's (Maihara et al. 1973). From the polarization angle aligned nearly along the Galactic plane, and the wavelength dependence of polarization well fitted by a power law (Nagata et al. 1994), it has been interpreted that the polarization is of interstellar origin dominated by dust that lies in the Galactic disk (e.g., Hough et al. 1978; Kobayashi et al. 1980; Lebofsky et al. 1982).

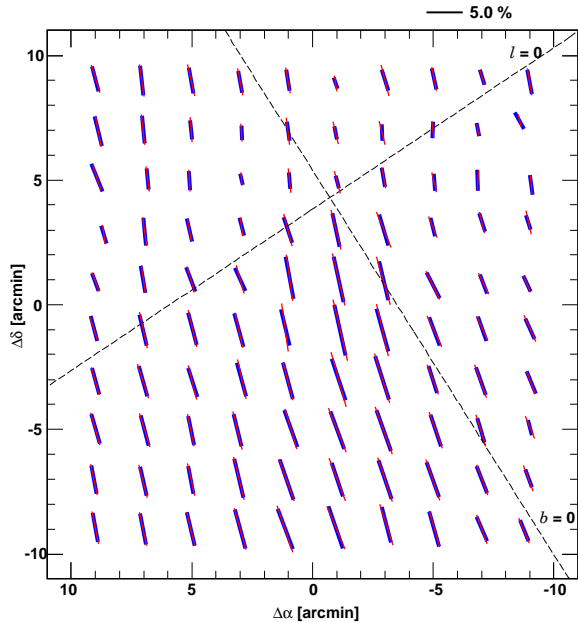


Fig. 9.— K_S -band polarization map derived from the blue-star component (P_B & θ_B : blue bars) and red-star component (P_R & θ_R : red bars).

One of the deepest NIR polarimetric observations toward the GC was carried out by Eckart et al. (1995) for a small field of $\sim 13'' \times 13''$. They established significant polarization for 160 sources fainter than 13 mag in the K band. The mean flux-weighted polarization is 4 % at 25° , nearly parallel to the Galactic plane. A similar result, $4.1 \pm 0.6\%$ at $30 \pm 10^\circ$, was also obtained by Ott et al. (1999). Eckart et al. (1995) concluded that most of the polarizations are caused via absorption by aligned dust grains in the Galactic plane.

A change of the magnetic field configuration along the line of sight toward the GC has been pointed out by Kobayashi et al. (1983). The diagram of position angles in the K band versus $H - K$ for 15 discrete sources (Fig. 5, Kobayashi et al. 1983) showed that the position angles are smaller and less ordered for sources with $H - K < 1.0$, while those with $H - K > 1.0$ are confined to a relatively narrow range around 20° . They concluded that this may indicate a change of the magnetic field direction at a distance corresponding to $H - K = 1.0$ (5 kpc or more according to their

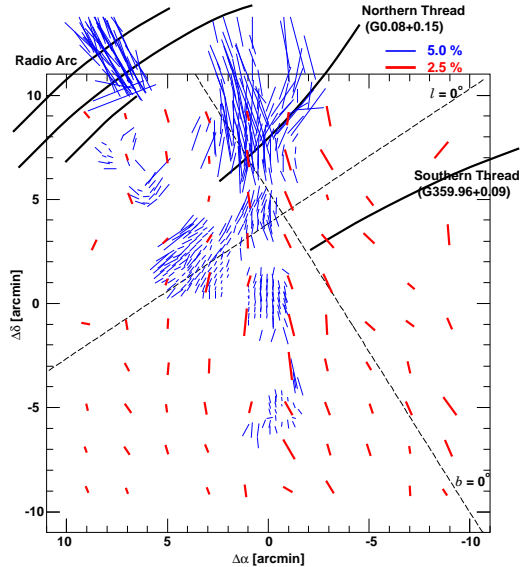


Fig. 10.— K_S -band polarization map derived from the Galactic center component (P_{R-B} & θ_{R-B} , red bars), where the polarization is detected with $P_{R-B}/\delta P_{R-B} \geq 2$. The polarization map at the center of our Galaxy derived from FIR/sub-mm observations (blue bars) is also shown. The length of the bars is proportional to the measured degree of polarization, and their orientation is drawn parallel to the inferred magnetic field direction. The FIR/sub-mm wavelengths data sets are from $60 \mu\text{m}$ & $100 \mu\text{m}$ polarimetry by Dotson et al. (2000), and $350 \mu\text{m}$ polarimetry by Novak et al. (2000) and Chuss et al. (2003, see also their Fig. 1). Some prominent radio filaments are shown as heavy dark lines.

calculation).

We can also identify a change of the position angle in the K_S bands at $H - K_S \sim 1.0$ (see Fig. 4). As shown in the color-color diagram in Fig. 1, most of the stars with $H - K_S \gtrsim 1.0$ have the color of giants (i.e., their unreddened positions are on the locus of giants), and the strong peak in the $H - K_S$ histogram (the top panel in Fig. 1) suggests that they are distributed in the Galactic bulge. Hence, this change of the position angle indicates a transition of the magnetic field configuration along the line of sight, between the Galactic disk and bulge.

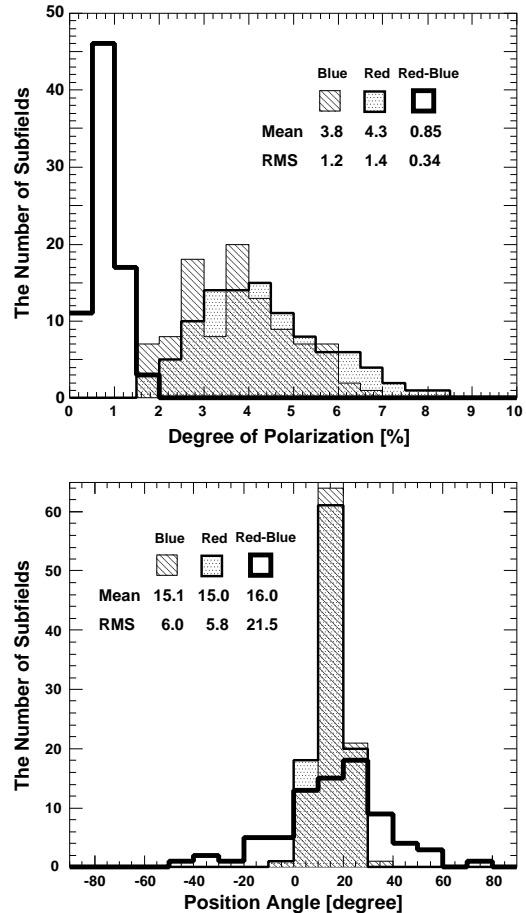


Fig. 11.— Top: Histograms of degrees of polarization for P_B (hatched), P_R (dotted), and P_{R-B} (white). Bottom: Histograms of position angles for θ_B (hatched), θ_R (dotted), and θ_{R-B} (white).

4.2. “Red” and “Blue” Stars and Their Separation in the Line of Sight

To discriminate between foreground disk stars and those in the Galactic bulge, the criterion $H - K_S = 1.0$ is applied in our analysis because most stars with $H - K_S > 1.0$ are attributed as giants in the Galactic bulge. The histogram of $H - K_S$ and the color-color diagram of point sources with photometric errors of less than 0.1 mag in the three bands are shown in Fig. 1. Nearby stars can be found around the giants’ and dwarfs’ loci (thick and thin curves) without reddening, while most of the redder stars, which are located at $H - K_S \gtrsim 1.0$ and $J - H \gtrsim 2.5$, have a color expected for

reddened giants. Toward the GC, the number of stars in the bulge is larger than in the exponential disk by a factor of ~ 50 (Wainscoat et al. 1992), and thus most of the stars at $H - K_S \gtrsim 1.0$ and $J - H \gtrsim 2.5$ are giants in the Galactic bulge.

The bottom panel of Fig. 8 shows the location of the red and blue stars in the K_S vs. $H - K_S$ color-magnitude diagram. The theoretical Padova isochrones (Girardi et al. 2002) for solar metallicity with an age of 10 Gyr are also plotted in the color-magnitude diagram. The isochrones are put at the distance of the GC (7.5 kpc; Nishiyama et al. 2006b) and shifted along the reddening vector ($A_{K_S}/E_{H-K_S} = 1.44$; Nishiyama et al. 2006a) with K_S extinctions of 0, 1, 2, 3, 4, and 5 mag. The distances to the red and blue stars are difficult to estimate accurately, since we do not know the distribution of the interstellar dust along the line of sight; however, most of the giants in the Galactic bulge can be detected for at least $K_S < 15$, and for these stars, we can find a clear peak in the $H - K_S$ histograms. Fig. 7 clearly shows that our observations are essentially equally sensitive to stars on the near ($H - K_S \lesssim 2.0$) and far ($H - K_S \gtrsim 2.0$) sides of the Galactic bulge for $H \leq 15.0$. The clear peaks found in the $H - K_S$ histograms are thus due to the spatial distribution of stars, not due to a distance effect. This indicates that $(H - K_S)_{\text{peak}}$ roughly corresponds to a real peak of the spatial distribution of giants along the line of sight. The color-magnitude diagram of Fig. 8 also tells us that a large number of blue stars are distributed around the distance where $1.0 \lesssim A_{K_S} \lesssim 2.0$, and most of the red stars are further than the distance which suffers from the extinction of $A_{K_S} = 2.0$.

From the distribution of $H - K_S$ color, we estimate the depth of the region where we have mapped the magnetic configuration shown in Fig. 10. For each sub-field, we calculated $H - K_S$ color differences between the peak in the $H - K_S$ histogram and the mean colors of blue and red stars, i.e., $(H - K_S)_{\text{peak}} - \langle (H - K_S)_{\text{blue}} \rangle$ and $\langle (H - K_S)_{\text{red}} \rangle - (H - K_S)_{\text{peak}}$. These color differences and corresponding extinction $A_{K_S\text{blue}} = 1.44 \times [(H - K_S)_{\text{peak}} - \langle (H - K_S)_{\text{blue}} \rangle]$ and $A_{K_S\text{red}} = 1.44 \times [\langle (H - K_S)_{\text{red}} \rangle - (H - K_S)_{\text{peak}}]$, where 1.44 comes from $A_{K_S}/E_{H-K_S} = 1.44$ (Nishiyama et al. 2006a), show the amount of dust extinction in the region where we have

obtained polarimetric information. First, the amount of extinction toward the peaks in the $H - K_S$ histograms can be calculated to be $A_{K_S\text{peak}} = 1.44 \times [(H - K_S)_{\text{peak}} - (H - K_S)_0]$, where the mean intrinsic color $(H - K_S)_0$ of red giants is assumed to be ~ 0.2 (see Fig. 8). This corresponds to the amount of extinction up to the GC in each sub-field. Next, the extinctions $A_{K_S\text{blue}}$ and $A_{K_S\text{red}}$ are converted to the actual distances from the GC, using a simple model. To make conservative estimates, we use the model by Davies et al. (1997), who derived a rather extended distribution of dust. Davies et al. (1997) showed that the extinction to the GC associated with cool diffuse interstellar dust can be calculated using

$$A = C \times \int_0^{R_0} e^{-r/\alpha_d} dr, \quad (3)$$

where $\alpha_d \approx 5.3$ kpc is a scale-length of the dust distribution in the radial direction, C is a constant depending on the wavelength and dust density, and R_0 is the distance between the GC and the Sun ($R_0 = 7.5$ kpc; Nishiyama et al. 2006b). The distances from the GC x_{blue} and x_{red} corresponding to $A_{K_S\text{blue}}$ and $A_{K_S\text{red}}$, respectively, can be estimated with the equations

$$\left(\int_0^{x_{\text{blue,red}}} e^{-r/\alpha_d} dr \right) / \left(\int_0^{R_0} e^{-r/\alpha_d} dr \right) = A_{K_S\text{blue,red}} / A_{K_S\text{peak}}.$$

We obtained the average and standard deviation of x_{blue} as 0.5 and 0.1 kpc, and those of x_{red} as 1.0 and 0.5 kpc, respectively. We found a long-side tail in the x_{red} histogram, which enlarges the average and the standard deviation. This estimation suggests that the polarization shown in Fig. 10 occurs between the average distances of $(R_0 - 0.5)$ kpc and $(R_0 + 1.0)$ kpc from the Sun, arising probably from the central 1–2 kpc region of our Galaxy.

In reality, the central part of the Galaxy harbors a strong concentration of gas and dust called the ‘‘Central Molecular Zone’’ ($R \lesssim 200$ pc; Morris & Serabyn 1996), which approximately corresponds to the concentration of stars called the ‘‘Nuclear Bulge’’ ($R \lesssim 300$ pc; Mezger et al. 1996; Serabyn & Morris 1996). According to Launhardt et al. (2002), stars belonging to the Nuclear Bulge dominate in the central part of the Galaxy (see their Fig. 14). Therefore, a large

portion of the stars we have detected is located in the Nuclear Bulge, and the polarization at the GC originates mostly within the central few hundred pc.

4.3. Magnetic Field Configuration at the GC

As shown in Fig. 10, we present the magnetic field configuration at the central region of our Galaxy by discriminating between the polarizations due to the disk and GC origin. The peak of the histogram of the position angle is $\sim 20^\circ$ (see Fig. 11), almost parallel to the Galactic plane. This coincidence, and the deficiency of θ_{R-B} around -60° , the angle perpendicular to the Galactic plane, show the basically toroidal geometry of the magnetic field. We cannot find a clear systematic dependence of position angle on Galactic latitude (from $b \approx -0^\circ.27$ to $+0^\circ.18$), suggesting that there is no systematic transition of the magnetic field direction in this region.

The direction of dust grain alignment at the GC has been investigated from polarized dust emission in the mid- and far-infrared and sub-mm wavelengths. The magnetic field implied by the emission is generally parallel to the Galactic plane in the circumnuclear disk (e.g., Werner et al. 1988; Morris et al. 1992; Hildebrand et al. 1993). As seen in Fig. 10, the magnetic field configuration we obtained at the GC shows a good agreement globally with those obtained by Dotson et al. (2000), Novak et al. (2000), and Chuss et al. (2003), which are the highest angular resolution polarimetry data sets in the FIR/sub-mm wavelengths. The local features also show an excellent agreement: an X-shaped feature extends from $(\Delta\alpha, \Delta\delta) = (-3', +10')$ down through $(+5', 0')$ (described in §3.1.4, Chuss et al. 2003) is also confirmed in our map. The configuration at $M-0.13-0.08$ around $(-1', -5')$ is also reproduced. The polarized FIR/sub-mm emission comes from molecular clouds, which are known to be located in the GC. Therefore we conclude that the position angles derived from our NIR polarimetry represent the direction of the aligned dust grains *in* the GC.

Chuss et al. (2003) has suggested that the magnetic field aligns generally perpendicular to the Galactic plane in low density regions, while the field has a toroidal configuration in high density

regions. They explain this correlation using the idea that in underdense regions, the magnetic field energy density can support itself against gravitational forces, preserving a primordial poloidal magnetic field. In overdense regions like molecular clouds, on the other hand, the gravitational forces are strong enough to shear the magnetic field into a direction parallel to the Galactic plane. In this context, lower density regions should have a poloidal configuration. However, in our vector map, the field shows a predominantly toroidal direction even at locations where the FIR/sub-mm emission is too weak for polarimetry [at the southeastern corner in Fig. 10, see also Fig. 1 in Chuss et al. (2003) and Fig. 2 in Novak et al. (2003).] The weak FIR/sub-mm emission suggests a paucity of dense clouds along the lines of sight, and the polarization in this direction can be considered to be interstellar in origin. Hence the “interstellar” magnetic field at the GC is dominated by a toroidal configuration, and the primordial poloidal magnetic field, if it existed, is not preserved today in this region.

Several radio filaments exist in our observed field, and three of them are prominent: the GC Radio Arc (Yusef-Zadeh et al. 1984), and the Northern and Southern Threads (also known as G0.08+0.15 and G359.96+0.09; Morris & Yusef-Zadeh 1985), which are shown in Fig. 10. Polarization studies have confirmed that the emission from the filaments is strongly linearly polarized, and that the internal magnetic field orientations are parallel to the long axes of the filaments (Tsuboi et al. 1986; Lang et al. 1999). The simplest interpretation of these observations, combined with the discovery of more filaments (e.g., LaRosa et al. 2004; Yusef-Zadeh et al. 2004), is that poloidal magnetic fields are pervasive throughout the central few hundred pc. Although the polarizations originating from the filaments cannot be detected in our observation, those toward the surrounding fields can be detected. The filaments have a width of less than $\sim 10''$ (Lang et al. 1999), and probably have a depth similar to their width. On the other hand, the size of the grids of our analysis is $2' \times 2'$, and the polarization shown in Fig. 10 is the average of $\sim 1-2$ kpc from the GC along the line of sight. Hence most of the stars we detected do not show a polarization originating from the filaments. However, we can detect the average

polarization near the line of sight toward the filaments. As shown in Fig. 10, most of the position angles of the grids including the filaments align nearly perpendicular to them rather than parallel. Therefore, Fig. 10 suggests that the average magnetic field has a toroidal configuration even around the sight-lines toward the filaments. We note again that the polarization is the average along the line of sight and does not originate from the area close to the filaments.

4.4. NIR Polarization as a New Tool for Mapping the GC Magnetic Field

We have shown that the polarization of starlight can be a probe of the magnetic field near the GC. Morris (1998) enumerated five different ways in which the magnetic field near the GC has been studied: morphology, polarization angle, Faraday rotation of the radio continuum, Zeeman effect, and polarized dust emission in FIR/sub-mm wavelengths. The polarization of starlight has not been employed for such investigations.

The optical polarization of starlight can trace the structure of the local magnetic field, but cannot detect stars near the GC due to large extinction. NIR polarimetry has been carried out toward the GC prior to our observations (see §4.1), but division of polarization into several components (e.g., originating from the Galactic disk and the central region) has not been done previously. The wide field-of-view of the NIR polarimeter SIRPOL, and the statistical treatment of tens of thousands of stars enable us to study the magnetic field near the GC; that is, the NIR polarimetry of starlight is a new way to investigate the magnetic field.

NIR polarimetry has the advantage of providing information about the magnetic field at locations where FIR/sub-mm emission is weak. NIR polarization of starlight is attributed to extinction along the line of sight by aligned dust grains, while FIR/sub-mm polarization is due to emission from the aligned dust. Hence, NIR polarimetry can investigate the magnetic field in regions where FIR/sub-mm polarimetry is absent, if background stars exist. This advantage is clearly shown in Fig. 10. We have detected polarization at positions where blue bars are not shown. The distribution of the position angles including such low emission regions shows a globally toroidal magnetic config-

uration at the GC.

5. SUMMARY

We have measured the near-infrared polarization of point sources toward the Galactic center (GC) in the $20' \times 20'$ region centered at Sgr A*. The difference in the Stokes parameters between stars at the close and far sides of the GC reveals the polarization originating from the central 1–2 kpc region of our Galaxy. The distribution of the position angle for the central region shows good agreement with those obtained from polarized emission of dust in the GC, showing that the near-infrared polarization of point sources can be used as a tool to investigate the magnetic field configuration of the GC. The position angles have a peak at $\sim 20^\circ$, which is almost parallel to the Galactic plane, suggesting a global toroidal magnetic field in the region.

We are grateful to Hiroshi Akitaya for his helpful comments, and Jun Hashimoto for his help with our analysis. We thank the staff of the South African Astronomical Observatory (SAAO) for their support during our observations. The IRSF/SIRIUS project was initiated and supported by Nagoya University and the National Astronomical Observatory of Japan in collaboration with the SAAO. SN is financially supported by the Japan Society for the Promotion of Science (JSPS) through the JSPS Research Fellowship for Young Scientists. This work was supported by KAKENHI, Grant-in-Aid for Young Scientists (B) 19740111, Grant-in-Aid for Scientific Research (A) 19204018, and Grant-in-Aid for Scientific Research on Priority Areas 15071204, and also supported in part by Grants-in-Aid for the 21st Century COE “The Origin of the Universe and Matter: Physical Elucidation of the Cosmic History” from the MEXT of Japan. This publication makes use of data from the Two Micron All Sky Survey, a joint project of the University of Massachusetts, the Infrared Processing and Analysis Center, the National Aeronautics and Space Administration, and the National Science Foundation.

REFERENCES

Chuss, D. T., et al. 2003, *ApJ*, 599, 1116

- Davies, J. I., Trewhella, M., Jones, H., Lisk, C., Madden, A., Moss, J. 1997, *MNRAS*, 288, 679
- Dotson, J. D., Davidson, J., Dowell, C. D., Schlenning, D. A., & Hildebrand, R. H. 2000, *ApJS*, 128, 335
- Eckart, A., Genzel, R., Hofmann, R., Sams, B. J., & Tacconi-Garman, L. E. 1995, *ApJ*, 445, L23
- Girardi, L., Bertelli, G., Bressan, A., Chiosi, C., Groenewegen, M. A. T., Marigo, P., Salasnich, B., & Weiss, A. 2002, *A&A*, 391, 195
- Hildebrand, R. H., Davidson, J. A., Dotson, J., Figer, D. F., Novak, G., Platt, S. R., & Tao, L. 1993, *ApJ*, 417, 565
- Goodrich, R. W. 1986, *ApJ*, 311, 882
- Hough, J. H., McCall, A., Adams, D. J., & Jameson, R. F. 1978, *A&A*, 69, 431
- Kandori, R., et al. 2006, *Proc. SPIE*, 6269, 159
- Kobayashi, Y., Kawara, K., Kozasa, T., Sato, S., & Okuda, J. 1980, *PASJ*, 32, 291
- Kobayashi, Y., Okuda, H., Sato, S., Jugaku, J., & Dyck, H. M. 1983, *PASJ*, 35, 101
- Lang, C. C., Morris, M., & Echevarria, L. 1999, *ApJ*, 526, 727
- LaRosa, T. N., Nord, M. E., Joseph, T., Lazio, W., & Kassim, N. E. 2004, *ApJ*, 607, 302
- Launhardt, R., Zylka, R., & Mezger, P. G. 2002, *A&A*, 384, 112
- Lebofsky, M. J., Rieke, G. H., Deshpande, M. R., & Kemp, J. C. 1982, *ApJ*, 263, L672
- Maihara, T., Okuda, H., & Sato, S. 1973, in *IAU Symposium no. 52, Interstellar Dust and Related Topics*, ed. Greenberg, J. M., & van de Hulst, H. C., 191
- Mezger, P. G., Duschl, W. J., & Zylka, R. 1996, *A&A Rev.*, 7, 289
- Morris, M., & Yusef-Zadeh, F. 1985, *AJ*, 90, 2511
- Morris, M., Davidson, J. A., Werner, M., Dotson, J., Figer, D. F., Hildebrand, R., Novak, G., Platt, S. 1992, *ApJ*, 399, L63
- Morris, M., & Serabyn, E. 1996, *ARA&A*, 34, 645
- Morris, M. 1998, in *IAU Symp. 184, The Central Regions of the Galaxy and Galaxies*, ed. Y. Sofue (Dordrecht: Kluwer), 331
- Nagashima, C., et al. 1999, in *Star Formation 1999*, ed. T. Nakamoto (Nobeyama : Nobeyama Radio Obs.), 397
- Nagayama, T., et al. 2003, *Proc. SPIE*, 4841, 459
- Nagata, T., Kobayashi, N., & Sato, S. 1994, *ApJ*, 423, L113
- Nishiyama, S., et al. 2006b, *ApJ*, 638, 839
- Nishiyama, S., et al. 2006a, *ApJ*, 647, 1093
- Novak, G., Dotson, J. L., Dowell, C. D., Hildebrand, R. H., Renbarger, T., & Schlenning, D. A. 2000, *ApJ*, 529, 241
- Novak, G., Chuss, D. T., Renbarger, T., Griffin, G. S., Newcomb, M. G., Peterson, J. B., Loewenstein, R. F., Pernic, D., & Dotson, J. L. 2003, *ApJ*, 583, L83
- Ott, T., Eckart, A., & Genzel, R. 1999, *ApJ*, 523, 248
- Persson, S. E., Murphy, D. C., Krzeminski, W., Roth, M., & Rieke, M. J. 1998, *AJ*, 116, 2475
- Serabyn, E., Morris, M. 1996, *Nature*, 382, 602
- Shibata, K., & Uchida, Y. 1986, *PASJ*, 38, 631
- Skrutskie, M. F., et al. 2006, *AJ*, 131, 1163
- Sofue, Y., & Handa, T. 1984, *Nature*, 310, 568
- Stetson, P. B. 1987, *PASP*, 99, 191
- Tokunaga, A. T. 2000, *Astrophysical Quantities*, 4th edition, ed. Cox, A. (AIP Press), p.143
- Tokunaga, A. T., Simons, D. A., & Vacca, W. D. 2002, *PASP*, 114, 180
- Tsuboi, M., Inoue, M., Handa, T., Tabara, H., Kato, T., Sofue, Y., & Kaifu, N. 1986, *AJ*, 92, 818
- Uchida, Y., Sofue, Y., & Shibata, K. 1985, *Nature*, 317, 699

Wainscoat, R. J., Cohen, M., Volk, K., Walker, H. J., & Schwartz, D. 1992, ApJS, 83, 111

Werner, M. W., Davidson, J. A., Morris, M., Novak, G., Platt, S. R., Hildebrand, R. H. 1988, ApJ, 333, 729

Yusef-Zadeh, F., Morris, M., & Chance, D. 1984, Nature, 310, 557

Yusef-Zadeh, F., Hewitt, J. W., & Cotton, W. 2004, ApJS, 155, 421